ACS APPLIED MATERIALS & INTERFACES

Research Article

www.acsami.org

Raman Characterization of Nanoparticle Transport in Microfluidic Paper-Based Analytical Devices (μPADs)

Rebecca Halvorson Lahr, Grant. C. Wallace, and Peter J. Vikesland*

Department of Civil and Environmental Engineering and Institute of Critical Technology and Applied Science (ICTAS), Virginia Tech, 418 Durham Hall, Blacksburg, Virginia 24060-0246, United States

Supporting Information

ABSTRACT: There is great interest in the use of microfluidic paper-based analytical devices (μPADs) for low-cost diagnostics. In this contribution, we illustrate the utility of Raman spectral imaging for both μPAD characterization and for quantification of the transport of applied reagents and analytes within these devices. We evaluated the transport of nanoscale particles within μPADs using a suite of differentially functionalized gold (AuNP) and silver (AgNP) nanoparticles with diameters of 8−64 nm. Nanoparticle transport within the cellulose matrix was characterized by collection of both Raman and surface-enhanced Raman spectroscopy (SERS) spectral maps that enabled differentiation of cellulose fibers and characterization of analyte deposition patterns. The transport of citrate (cit), BSA, PEG, PVP, and DNA functionalized AuNP and AgNP in wax-printed μPADs was primarily affected by nanoparticle surface chemistry rather than particle size or core composition. Sample pH (3−10) influenced the transport of 15 nm BSA-cit-AuNP, but not 15 nm cit-AuNP, because of the effects of solution pH on the charge and conformation of BSA. Derjaguin, Landau, Verwey, and Overbeek theory (DLVO) and extended DLVO (xDLVO) theory are used to explain the collected experimental results.

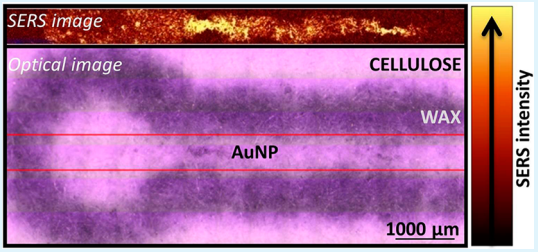

KEYWORDS: *nanoparticle transport, cellulose, wax-printed microfluidic paper based analytical devices (μPADs), surface-enhanced Raman spectroscopy (SERS), DLVO, Hamaker constants*

INTRODUCTION

Microfluidic analytical devices (μPADs) have been developed for the detection of glucose, proteins, cholesterol, metals, and microorganisms via colorimetric, electrochemical, chemiluminescent, and surface-enhanced Raman spectroscopy (SERS); however, development of these diagnostics is far from optimized.[1−4] There is particular interest in the application of μPADs for detection of nanoparticulate materials (e.g., virus) for resource limited or point-of-use applications.[5] Because they are of comparable scale to the cellulose fibers within the μPAD the transport of nanoparticulate analytes is expected to differ relative to soluble analytes. Although prior work has illustrated the utility of μPADs for detection of nanoscale materials, there have been no studies to date that have systematically evaluated the factors that dictate nanoparticle fate within μPADs. Past studies suggest that nanomaterial transport will result in highly heterogeneous deposition patterns because of capillary transport during the drying process and the "coffee ring" effect.[2,6] To date, while a substantial body of work has examined nanoparticle transport in porous media,[7] there has been little work characterizing such transport within cellulose matrices. The only study in this area focused exclusively on deposition of TiO_2-based dyes within paper pulp.[8] The present manuscript represents, to our knowledge, the first attempt to track deposition patterns of nanoscale objects in μPADs as a function of surface functionalization.

Normal Raman spectroscopy is readily used to identify polarizable molecules based on their ability to inelastically scatter light.[9] The technique is especially useful for samples with high concentrations and little fluorescence. Gold (AuNP) or silver (AgNP) nanomaterial transport within μPADs can be visually tracked to some degree by the visible pink or green colors that arise due to their localized surface plasmon resonance (LSPR) absorbances near 520 and 400 nm, respectively.[10−12] SERS can record images of noble-metal nanoparticle deposition quickly and efficiently at low concentrations in transparent or translucent media, as long as the laser wavelength used to produce the Raman spectra overlaps with the LSPR of the nanoparticles, thus producing a Raman signal enhancement.[13−16] Raman spectral imaging of μPADs provides more sensitive and specific information than colorimetric detection and is more versatile and rapid than electron microscopy. To date, Raman imaging has been used to record nanoparticle aggregation in aqueous systems and to map cellular components but has not been fully employed to characterize μPADs.[17−19] Although nanomaterials are frequently used in μPADs,[5,20−22] their transport properties and deposition patterns in μPADs generally remain unexplained. Herein, wax-printed μPADs were characterized using Raman

Received: February 6, 2015
Accepted: April 8, 2015
Published: April 8, 2015

DOI: 10.1021/acsami.5b01192
ACS Appl. Mater. Interfaces 2015, 7, 9139−9146

Table 1. Characteristics of Nanoparticles Applied to Wax-Printed Papers, Including AgNP Coated with Polyvinylpyrrolidone (PVP) and Citrate (cit) Reduced AuNP Coers Functionalized with Bovine Serum Albumin (BSA), Polyethylene Glycol (PEG) with Various End Groups, Malachite Green Isothiocyanate (MGITC), Rhodamine B Isothiocyanate (RBITC), and Oligonucleotides (DNA)[a]

sample	core size (nm)	hydrodynamic diameter (nm)	PDI[b]	zeta potential (mV)	pH	electrophoretic mobility (μm·cm/(V s))	conductivity (mS/cm)	refs
15 nm cit-AuNP	15 ± 7	18 ± 0.1	0.32	−58.9 ± 9.7	6.4	−3.1 ± 0.5	0.4	26, 27
46 nm cit-AuNP	46 ± 5	36 ± 0.2	0.25	−31.0 ± 17	3.5	−2.4 ± 1.3	0.3	27, 28
15 nm BSA-cit-AuNP	15 ± 7	26 ± 0.2	0.19	−31.4 ± 16	8.1	−1.6 ± 0.8	2.1	29
46 nm BSA-cit-AuNP	46 ± 5	58 ± 1.2	0.25	16.7 ± 9.8	4.4	1.3 ± 0.8	0.2	27, 29
64 nm BSA-cit-AuNP	64	58 ± 0.1	0.43	18.6 ± 13	4.2	1.5 ± 1.0	0.2	29
46 nm OCH_3−PEG-cit-AuNP	47 ± 5	126 ± 2	0.47	−51.3 ± 9.2	6.1	−2.7 ± 0.5	0.002	30
46 nm COOH-PEG-cit-AuNP	47 ± 5	78 ± 1.5	0.4	−36.9 ± 8.5	5.8	−1.9 ± 0.4	0.002	30
46 nm OCH_3/COOH-PEG-cit-AuNP	47 ± 5	91 ± 1.4	0.42	−48.7 ± 10	6.3	−2.5 ± 0.5	0.002	30
46 nm MixPEG-MGITC-cit-AuNP	47 ± 5	84 ± 1.2	0.25	−50.6 ± 11	5.8	−2.6 ± 0.6	0.02	30
46 nm MixPEG-RBITC-cit-AuNP	47 ± 5	88 ± 2.3	0.25	−55.9 ± 15	5.7	−2.9 ± 0.8	0.004	30
46 nm DNA-MixPEG-MGITC-cit-AuNP	47 ± 5	91 ± 2.5	0.34	−55.2 ± 8.2	6.5	−2.9 ± 0.4	0.009	30
40 nm PVP10K-AgNP	41	65 ± 1.3	0.28	−18.9 ± 13	6.6	−1.0 ± 0.67		31
40 nm PVP55K-AgNP	42 ± 10	78 ± 0.6	0.18	−41.2 ± 17	8.3	−2.2 ± 0.9		32, 33
8 nm PVP55K-AgNP	8 ± 5	79 ± 1.5	0.41	−32 ± 17	9.5	−1.7 ± 0.9		32, 33
8 nm PVP10K-AgNP	7 ± 3	56 ± 2.2	0.44	−33.9 ± 17	9.2	−1.8 ± 0.9		31, 32, 34

[a]Supporting Information Table S1 contains nanoparticle synthesis details. Standard deviations of replicate measurements are provided. [b]PDI = polydispersity index.

spectroscopy and the transport of nanoparticles with various surface coatings was quantified using Raman and SERS. The results exemplify the utility of Raman spectral imaging for μPAD characterization. Nanoparticle transport is discussed in terms of electrostatic, van der Waals, Lewis acid−base, and steric interactions between the nanoparticles and cellulose.

MATERIALS AND METHODS

$HAuCl_4$ was purchased from MP Biomedical; 5 kDa HS-PEG-OCH_3 and 3.4 kDa HS-PEG-COOH were purchased from NANOCS; and rhodamine B isothiocyanate (RBITC), malachite green isothiocycante (MGITC), and oligonucleotide (5′-NH2-TCGGC ACGTT CTCAG TAGCG CTCGC TGGTC ATCCC ACAGC TACGT-3′) were from Invitrogen. *N*-hydroxysulfosuccinimide (sulfo-NHS) and bovine serum albumin (BSA) were purchased from Sigma-Aldrich; 1-ethyl-3-[3-(dimethylamino)propyl]carbodiimide hydrochloride (EDC) was obtained from Fluka; and *Pseudokirchneriella subcapitata* cultures were from Marinco Bioassay Laboratory Aquaculture. Dissolved organic matter (DOM) from the Great Dismal Swamp in North Carolina was filtered to remove all constituents larger than 0.45 μm, freeze-dried, and rehydrated prior to use.[23] Nanopure water (>18 MΩ cm) was obtained from a Barnstead Nanopure water purification system and was used for all experiments.

Substrate Preparation and Characterization. Wax-printed μPADs with a 1.2 mm channel width, 0.3 mm wax wall thickness, 3 mm sample spot diameter, and 5 cm channel length (dimensions of designs before heating; Supporting Information Figures S1 and S2) were designed in Adobe Photoshop CS and printed on Whatman grade 1 chromatography paper using a Xerox ColorQube 8570 printer, a newer model that has succeeded the Xerox Phaser described in the pioneering μPAD papers.[24,25] After printing, the paper was heated wax-side up on a digital hot plate at 150 °C for 60 s, wax side down for 30 s, and wax side up for another 30 s. Wax printed papers were characterized using a LEO (Zeiss) 1550 field emission scanning electron microscope (FESEM), a FTA125 goniometer, and a Sony Cyber-shot DSC-S750 digital camera. Prepared wax-printed channels were placed in Petri dishes with the printed side up for testing with nanoparticle suspensions.

Sample Description and Characterization. Previously reported nanoparticle synthesis methods were carried out as described in the Supporting Information (Table S1). Nanoparticle core diameters were determined using ImageJ (NIH, version 1.46) to size electron micrographs obtained with either a Zeiss 10CA transmission electron microscope (TEM) with an AMT Advantage GR/HR-B CCD Camera System or a JEOL JEM 1400 TEM with a Gatan Orius CCD camera controller (Table 1). Many of the test nanoparticles were produced via citrate reduction and as such are identified using the term cit to reflect residual citrate at the nanoparticle surface. Additional surface coatings applied over the citrate layer are identified as follows XXX-cit-yyNP where XXX is the overlayer (e.g., PEG, BSA) and yy is the specific nanoparticle type (e.g., Ag or Au). A Varian Cary 5000 UV−vis-NIR spectrophotometer documented the surface plasmon resonance band locations and the stability of the nanoparticle solutions prior to use (Supporting Information Figure S3). An Accumet AB15 Plus pH Meter (Fisher Scientific) measured pH as controlled by dropwise addition of 1 M HCl, 1 M NaOH, or 10 M NaOH. A Malvern Zetasizer NanoZS instrument and autotitrator measured the hydrodynamic diameter (z-average), electrophoretic mobility, and conductivity of the nanoparticle solutions (Table 1). The autotitrator monitored pH with an accuracy of 0.2 pH units, collected measurements every 0.5 pH units, and used 0.1 M NaOH and 0.1 M HNO_3 as titrants. The transport behavior of various nanoparticles in aqueous solutions applied to μPADs was contrasted with that of soluble amaranth dye, 50 g/L $HAuCl_4$, and Great Dismal Swamp DOM.

Nanoparticle Transport within Wax-Printed Cellulose. Aliquots of 2 μL of each nanoparticle suspension or the three soluble species (amaranth, $HAuCl_4$, and DOM) were pipetted into μPAD sampling spots printed-side up in a Petri dish open to the air, and capillary action carried reagents through the paper fibers. The pH of the nanoparticle suspensions was adjusted with concentrated NaOH or HCl to obtain samples of amaranth, DOM, 15 nm cit-AuNP, and 15 nm BSA-cit-AuNP at pH values from 3 to 10 before application onto the μPADs. After it was dried for at least 10 min at room temperature, digital photographs of each channel were taken. Channels were then rinsed three times with 4 μL of nanopure water, dried for >10 min at room temperature, and photographed again. A ruler was included in all

DOI: 10.1021/acsami.5b01192
ACS Appl. Mater. Interfaces 2015, 7, 9139−9146

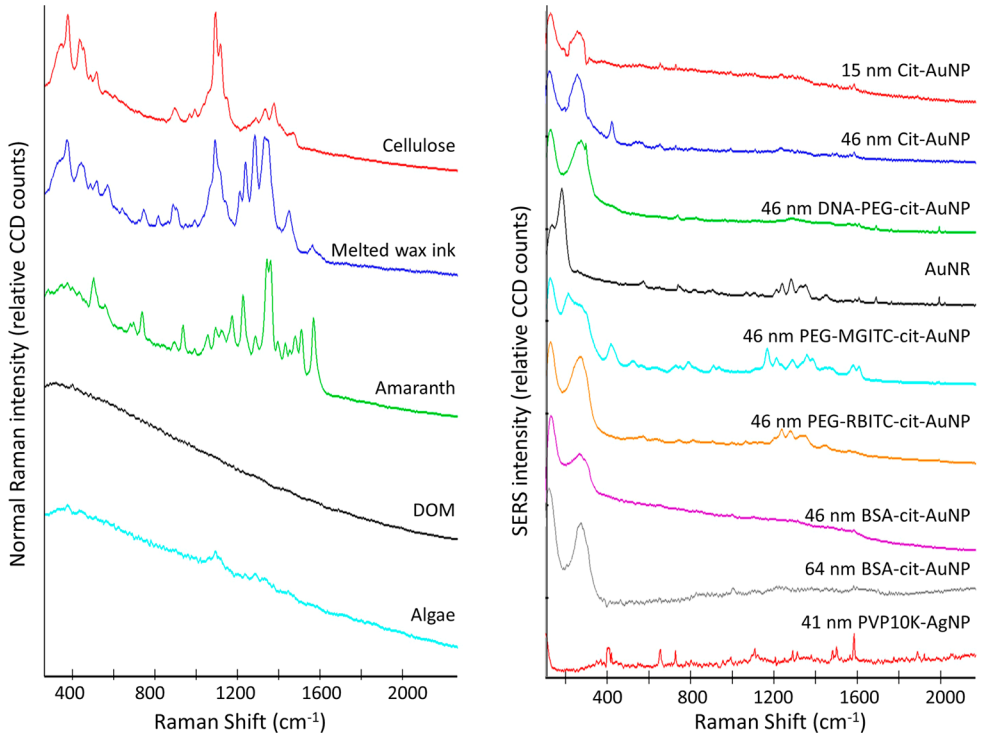

Figure 1. Raman (left panel) and SERS (right panel) spectra of each analyte were collected in the presence of cellulose. Instrument parameters are included in Supporting Information Table S3.

photographs to facilitate travel distance measurements with ImageJ. Analyte deposition patterns in wax-printed paper channels were imaged by Raman spectroscopy with a WITec Alpha500R Raman UHTS300 spectrometer, DU 401 BR-DD CCD camera, 785 nm laser, 300 grooves/mm, 10× microscope objective, and 0.05−115 mW of laser power. A Raman band specific to each analyte was chosen using Figure 1, and the intensity of that peak was used to generate Raman XY images from thousands of Raman spectra collected across a wax-printed paper channel. Typically for the Au and Ag nanomaterials the Raman band at 55−398 cm^{-1} was the most intense, generating sufficient SERS signal in 0.05 s per spectrum. Peaks in the region near 120 and 260 cm^{-1} reflect Au surface−halide stretching modes (Supporting Information Table S2).[35,36] For a 785 nm laser and 10× objective with a numerical aperture of 0.3 positioned over a dry sample, the region probed by the laser per spectrum is ≈1.6 μm in the lateral direction and ≈17.4 μm in the axial direction.[37,38]

RESULTS AND DISCUSSION

Wax-Printed Paper Characterization. Whatman grade 1 chromatography paper is an ideal substrate for μPADs because it is widely available, cheap, well characterized, and compatible with commercially available wax printers. Chromatography paper produces a clear Raman spectrum with relatively few peaks and little fluorescence because of its purity and lack of additives (Figure 1).[25,39] This bibulous paper is composed of a 3D mat of intertwined cellulose fibers with a negative zeta potential at all pH values examined (Table 1).[40] The Xerox ColorQube printer uses a wax-based ink that successfully constrains nanoparticles and aqueous solutions within the wax channels. (The Supporting Information includes wax and μPAD characterization (Tables S4 and S5 and Figures S4 and S5).)[25,41,42] Channel dimensions were selected to produce the most consistent fluid transport and the strongest, most concentrated SERS signals (Supporting Information Figure S6).

Fluid Transport within Wax-Printed Channels. Upon pipetting an aqueous sample onto the sampling spot of a wax-printed paper channel, a large liquid droplet forms. Constrained by surface tension and hydrophobic interactions between wax and water, the droplet feeds the sample into the water-sorbing cellulose channel. Analytes within a sample (i.e., amaranth dye, $HAuCl_4$, DOM, nanomaterials) can be transported down the channel with the water phase, deposited onto the cellulose fibers, or drawn into the wax boundary layer by hydrophobic interactions. The travel distances of water-soluble amaranth, $HAuCl_4$, and DOM applied to cellulose in 2 μL sample aliquots were limited only by the water travel distance. This result, observed previously for soluble dyes,[25] indicates that water-soluble materials prefer to remain in the aqueous phase during transport rather than interacting with the wax or cellulose phases. These soluble species move and accumulated at the channel ends when the μPADs were rinsed with 4 μL aliquots of nanopure water added to the sample spotting zone (Supporting Information Figure S7). Additional 4 μL rinse steps did not fully remove the amaranth color from the cellulose, thus indicating that although the amaranth dye has an affinity toward the aqueous phase, some dye does deposit within the cellulose matrix.

The measured range of travel distances for amaranth over the course of a year varied from 1.7 to 3.3 cm with a mean of 2.3 cm and a standard deviation of 0.5 cm. As these experiments were carried out on a lab bench, such variation was expected due to humidity, temperature, airflow, imperfections in the wax-printed paper, differences in the direction of the cellulose fibers, inconsistent contact with the underlying substrate, and human error.[25,43] To account for day to day fluctuations in capillary flow, the measured nanoparticle travel distances were normalized to the measured travel of the amaranth dye. In essence, retention factors were calculated as traditionally used

DOI: 10.1021/acsami.5b01192
ACS Appl. Mater. Interfaces 2015, 7, 9139−9146

in paper chromatography, with amaranth dye acting as a tracer to record the distance of fluid travel.[44] Prior to such normalization, standard deviations were low for sets of the same sample tested on the same day and high for sets tested on different days. Once this normalization scheme was employed, average travel distances for each analyte were comparable throughout the study.

Nanoparticle Deposition Patterns. When nanoparticle analytes travel through wax-printed paper channels they are influenced by the mobile phase (water), the stationary phase (cellulose), the channel boundaries (wax), the underlying substrate, and the overlying air (temperature, humidity, air flow). Microscope images, normal Raman spectral maps, and SERS spectral maps capture detailed information concerning the cellulose fibers and the analytes applied to the channels (Figure 2 and Supporting Information Figure S8). Optical and

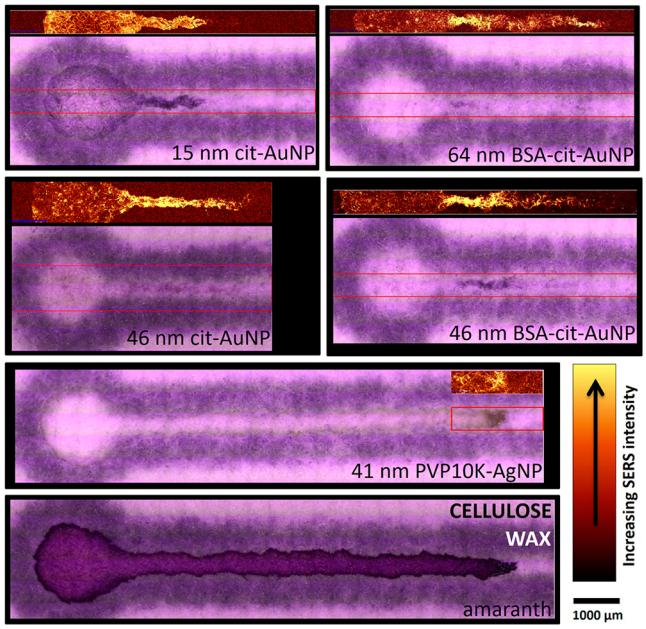

Figure 2. Optical microscope images (purple) and the corresponding SERS spectral maps record nanoparticle deposition patterns within narrow wax-printed channels of 0.8 mm width. Normal Raman spectral maps image the topography of the cellulose fibers and deposition patterns of fluorescent species such as algal cells, even within the same wax-printed paper channel (Supporting Information Figure S7), but the SERS spectral maps shown here were generated with a much lower laser power such that only nanomaterials display spectra. Images were collected with a 10× microscope objective, 785 nm laser, < 1 mW of laser power, 300 grooves per mm grating, 0.05 s per spectrum, and a resolution of 5 μm per spectra in the lengthwise channel direction by 10 μm per spectra wide. Raman spectral maps were generated based upon the intensity of the 55−398 cm^{-1} Raman signal. Particle size influences SERS signal intensity, so intensity scales are not constant for all images. Both PVP-AgNP and amaranth dye partition toward the wax layer and also travel far down the cellulose channel as demonstrated by wax-channel outlines of PVP-AgNP and amaranth captured in microscope images and Raman spectral maps.

Raman images delineate the channels because of the black pigment within the wax-based ink and its Raman signal. In addition, normal Raman spectral images depict the topography of the cellulose fibers by documenting the 1052−1171 cm^{-1} peak that occurs due to the C−C and C−O stretching modes of cellulose.[45] Sample fluorescence often challenges Raman spectral acquisition due to the inherent strength of the fluorescent signal that can overshadow the comparatively weaker Raman signal.[9] Experiments with algal cells, however, indicate that is possible to use their inherent fluorescence[46] to track their deposition locations within the wax-printed paper channel (Supporting Information Figure S8). As shown, these large cells are barely transported outside of the sample application zone. Impressively, the Raman spectrometer, with a 785 nm laser, is sensitive enough to record the normal Raman signals of the underlying cellulose fibers on top of the fluorescence of the algal cells in the channels. Such capabilities illustrate the utility of the method to document the transport and deposition of fluorescent or Raman active species within μPADs.

Nanomaterial deposition patterns were recorded both photographically and as SERS XY images at much lower laser powers (i.e., <5 mW) than typically required for normal Raman imaging (i.e., >100 mW) as indicated in Supporting Information Table S3. The collected images demonstrate that amaranth dye and 41 nm PVP10K-AgNP partition toward the boundary layer, but travel further along the channel than cit-AuNP or BSA-cit-AuNP (Figure 2). This result suggests that the amaranth and 41 nm PVP10K-AgNP have higher affinities to both the wax and the water than to the cellulose fibers. cit-AuNP and BSA-cit-AuNP remain in the center of the channels when they travel, maintaining minimum interaction with the wax boundary layer, as demonstrated by SERS spectral maps (Figure 2). Both the PVP and amaranth dye have nonpolar moieties within their molecular structures that facilitate their interaction with the wax (the wax composition is proprietary, but contains a hydrophobic hydrocarbon mixture or polymer; Supporting Information Table S4). The carboxylic acid groups on citrate lend it the capacity to hydrogen bond with cellulose. BSA protein generally folds such that sufficient hydrophilic groups are exposed to the solution to make the molecule stable in water; these hydrophilic functional groups would have a greater affinity for cellulose than the nonpolar wax boundary layer.[47,48]

Nanoparticle Travel within Wax-Printed Channels. Nanoparticle transport distances were not substantially affected by either nanoparticle size or core composition. However, they were greatly affected by the nanoparticle surface coating, with cit-AuNP depositing in or near the sampling spot and PVP or PEG coated particles traveling further along the channel, but rarely as far as the amaranth dye (Figure 3). After the initial sample was added to the channel and allowed to dry (approximately 10−30 min), three rinses of 4 μL of nanopure water had no influence on the transport distance of any of the nanoparticles at any pH except the 8 nm PVP10K-AgNP particles that traveled similarly to amaranth after rinsing (Supporting Information Figure S9). This result indicates that drying mediated nanoparticle adhesion is practically irreversible. Such an outcome has important implications for μPAD use for analysis of particulate materials as it indicates that designs must ensure that analytes are completely transported to a defined detection zone during the period that the μPAD is fully wetted.

Transport of amaranth, DOM, 15 nm cit-AuNP, and 15 nm BSA-cit-AuNP were tested at pH values between 3 and 10. Only the transport of 15 nm BSA-cit-AuNP was influenced by pH, depositing in or near the sampling spot at pH 3 and traveling half the length of the channel at pH 6−10 (Supporting Information Figure S10). BSA undergoes a structural

DOI: 10.1021/acsami.5b01192
ACS Appl. Mater. Interfaces 2015, 7, 9139−9146

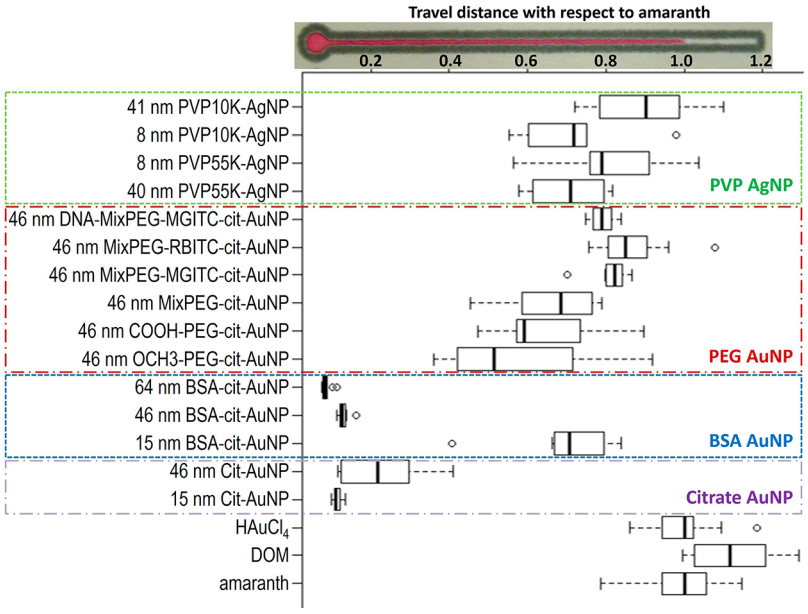

Figure 3. Nanoparticle transport distances relative to soluble amaranth dye without rinse steps in wax-printed channels on chromatography paper. The boxes represent the first and third quartile, with a bold line at the median. The smallest or largest sample measurement within 1.5 times the box size are represented by the whiskers.[49]

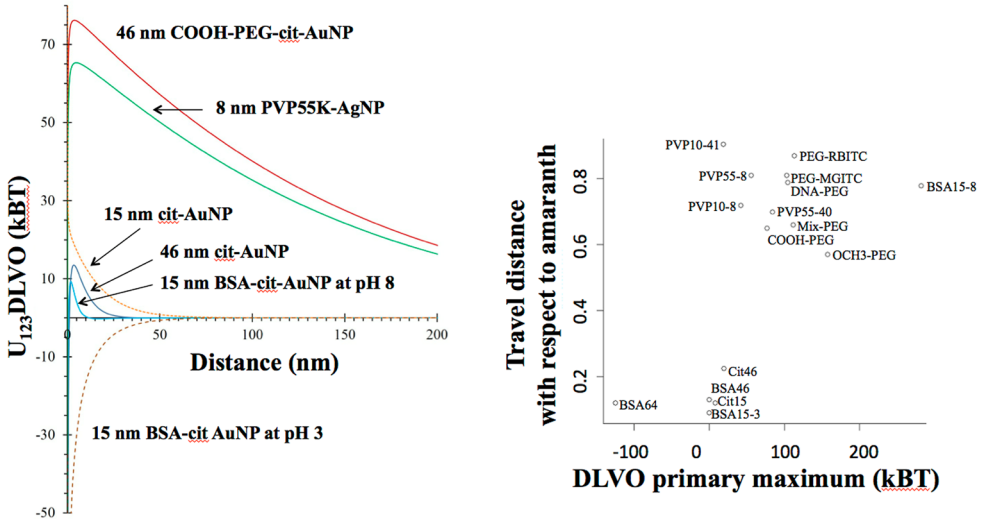

Figure 4. DLVO interaction energies for a nanoparticle approaching a cellulose surface were compared to travel distance. Nanoparticles that do not travel in wax-printed cellulose have low DLVO interaction energy barriers. Low ionic strength in nanoparticle solutions that include centrifugation steps and resuspension in water causes broadening and an increase of the primary maximum due to extension of the electrical double layer about the particle.[58] Additional DLVO plots and discussion of Hamaker constants are included in the Supporting Information.

conformation and zeta potential transition from positive at pH < 4 to negative at pH > 5.[47] Negatively charged particles repel negatively charged cellulose fibers,[40] and because opposite charges attract the positively charged BSA particles (low pH) deposit in the cellulose stationary phase. Analyte travel is influenced by pH when the charge, functional groups, conformation, or aggregation state of either interacting surface is affected by solution pH.[50] Although pH had no effect on the movement of 15 nm cit-AuNP, these particles aggregated at basic pH after 5 min of drying time as identified by a color change from bright red to purple within the paper.[12] Such aggregation must be considered when utilizing μPADs for nanoparticulate analytes.

Forces Influencing Analyte Transport. Analyte transport in a cellulose matrix is influenced by van der Waals, electrostatic, Lewis acid–base, and steric forces, as described by Derjaguin, Landau, Verwey, and Overbeek theory (DLVO) and extended DLVO (xDLVO).[51−54] DLVO provides a semiquantitative means to consider interactions between colloids and surfaces as a function of distance with insight into Lifshitz–van der Waals and electrostatic colloidal interactions. xDLVO extends DLVO analysis to include terms for Lewis acid–base and steric interactions, at the cost of simplicity and established experimental techniques to parametrize models for nanoparticles with thick surface coatings. DLVO calculations have been valuable in colloid science for modeling coagulation and flocculation, membrane fouling,

DOI: 10.1021/acsami.5b01192
ACS Appl. Mater. Interfaces 2015, 7, 9139−9146

protein immobilization, TiO_2 dye deposition in paper pulp, and transport of colloids in nanofluidic devices; thus it may provide insight into Lifshitz–van der Waals and electrostatic forces between noble-metal nanomaterials and μPADs.[8,55−57] Nonetheless, perspective must be maintained as to the subjective estimates of the Hamaker constant, the assumptions that surfaces are smooth and the particles are spherical, and the known pitfalls of calculating surface potential from zeta potential.[52]

Electrostatic and van der Waals Forces. Estimates of Lifshitz–van der Waals and electrostatic colloidal interactions were computed using measured particle sizes (TEM core size and DLS hydrodynamic diameter), measured zeta potential, estimated Hamaker constants, and estimated ionic strength (see the Supporting Information for details). For particle coatings considered thicker than the range of van der Waals forces (estimated from TEM images, hydrodynamic diameter measurements, and the molecular weight of the coating) the Hamaker constant of the coating was used instead of that of the metal core (all particles except cit-AuNP, Supporting Information contains additional details; Supporting Information Figure S11).[52] Correlations between nanoparticle transport distance and the core size, coating thickness, hydrodynamic diameter, zeta potential, ionic strength, or conductivity did not exist. As expected, particles that traveled minimally in the cellulose channels had small (<15 kT) primary maximum DLVO interaction energy barriers between the nanoparticle and cellulose (bottom left of Figure 4). Particles with high (>75 kT) primary maximum values were expected to resist interaction with cellulose and instead travel far with the mobile aqueous phase (top right of Figure 4. Despite imprecise and variable ionic strength estimates, extrapolation of surface potential from zeta potential, and the lack of precise Hamaker constant approximations, the trend generally holds when Hamaker constants of the coatings are used instead of that of the metal core. The fate of PVP-AgNPs typically cannot be explained by DLVO, and therefore, it is not surprising that despite their tendency to travel far in the cellulose, these particles have inconsistent DLVO primary maximum values between the two distinct groupings (20–85 kT). Furthermore, DLVO suggests that once a particle overcomes the primary maximum, deposition is irreversible.[52,58] As noted previously, irreversible deposition was observed in that the nanoparticles (excluding 8 nm PVP10K-AgNP) could not be rinsed down the channel after the initial drying period.

Lewis Acid–Base Interactions. Forces that influence transport and deposition, but are not included in traditional DLVO theory include Lewis acid–base forces and steric hindrance.[51,52,59] Lewis acid–base effects arise from polar interactions and encompass the terms "hydrophobic interaction" and "hydration pressure" often used to explain forces that cause particles to contradict DLVO.[51] Although Lewis acid–base interactions decay exponentially in aqueous solutions for lengths >0.1 nm, they can be stronger than electrostatic and van der Waals forces by 2 orders of magnitude.[51] As described by van Oss, the distinction between dipole–dipole interactions (Lifshitz-van der Waals component of DLVO) and electron-donor-electron-acceptor (Lewis acid–base component of xDLVO) interactions is oftentimes blurry.[51] PEG has been characterized to exhibit strong dipole interactions, strong dispersion forces, and only moderate hydrogen bonding when considered as a stationary phase for chromatography. Thus, the contribution of xDLVO forces for PEG are not expected to be as strong as for analytes that exhibit strong hydrogen bonding. PVP forms hydrogen bonds with cellulose through the carbonyl group.[60−63] However, PVP-AgNP does not deposit in the cellulose, but instead travels with the aqueous phase. Thus, other forces are at play, such as the predicted electrostatic repulsion, the observed affinity of PVP-AgNP for the wax phase, and the observed affinity of PVP-AgNP for the moving water phase (Figure 2).

Steric Forces. Steric repulsion is defined by Prime and Whitesides in terms of (1) compression of a polymer coating upon contact with a second particle or surface and (2) solvent expulsion from a polymer layer upon compression.[64,65] Steric repulsion is frequently cited as an important stabilizing force for polymer coated nanoparticles, especially for PEG and PVP coatings.[33,65−68] xDLVO has improved estimates of attachment efficiency for a variety of polymer coated nanoparticles by adding a term encompassing electrosteric repulsion and the decrease of friction force obtained using Oshima's soft particle analysis, and these improvements were observed despite the use of particle core Hamaker constants to describe particles with coatings up to 0.7–70 nm, thicknesses beyond the typical range of van der Waals attraction.[52] Considering the definition of steric repulsion given by Jeon and Prime, the comparative compressibility of PVP and PEG likely causes the observed difference in DLVO fit.[64,65] The pyrrole ring in PVP makes it a much more rigid molecule than PEG, such that compression of PVP is a more energy intensive process than for PEG.[68,69] This idea is discussed in terms of poly(ethylene oxide) by Jeon et al.; much like a rubber ball, surface compression of a poly(ethylene oxide) coating on a nanomaterial surface acts to spring proteins away upon approach.[64] Furthermore, PVP polymers blended with PEG also generally transmit water vapor and have higher swellability,[70] suggesting that PVP coatings are less accessible to any constituents of the water phase and that more energy would be required to expel upon compression any water that did make it into the PVP coating. Therefore, a steric term is expected to increase the primary maximum for PVP to a larger extent than any of the other coatings.

FUTURE OUTLOOK

μPADs employing nanomaterial based signal output offer rapid detection of a wide array of analytes in a portable, cheap, and effective manner. Imaging and understanding nanomaterial transport characteristics within μPADs will facilitate production of μPADs that either incorporate nanoparticles within their design or are developed for nanoparticle analysis. Raman spectroscopy and SERS provide a versatile, user-friendly tool for tracking analytes, reagents, and noble-metal nanoparticles in paper, polymer, or surface coatings with minimal sample prep. SERS spectra were analyzed herein simply to detect the transport distance of a single type of nanoparticle; work has been published demonstrating the deconvolution of spectra from each pixel of a SERS spectral image into several components (i.e., cellulose, nanoparticle core, nanoparticle coating, a second nanoparticle type), thus producing images for each component.[71,72] A tremendous amount of information can be obtained from each SERS spectral image and this will be the topic of future investigation. Furthermore, portable hand-held Raman spectrometers are commercially available for field μPAD assays. The most reproducible results for μPAD field deployable diagnostics will be obtained with well-defined devices, in which user error and sample deposition inconsistencies are minimized. Although the core identity remains

DOI: 10.1021/acsami.5b01192
ACS Appl. Mater. Interfaces 2015, 7, 9139−9146

important from a toxicity end point because, for example, silver ions are known to leach from AgNP, it is clear that nanoparticle surface coatings heavily influence particle deposition in a cellulose matrix. For particles with thick coatings that make up the bulk of the nanoparticle, especially for coatings thicker than the range of van der Waals forces, DLVO theory best explains the results if the nanoparticles are modeled as if they were composed of their surface coatings rather than their metal cores. Better estimates of model inputs (such as Hamaker constant) that are difficult to measure must be developed to improve the accuracy of transport models and thus aid in development of μPADs employing nanomaterials for detection or separation.

■ ASSOCIATED CONTENT

Supporting Information

Detailed discussion of AuNP synthesis and characterization, μPAD production and characterization, and DLVO calculation details. This material is available free of charge via the Internet at http://pubs.acs.org.

■ AUTHOR INFORMATION

Corresponding Author

*E-mail: pvikes@vt.edu. Phone: 540-231-3568. Fax: 540-231-7916.

Notes

The authors declare no competing financial interest.

■ ACKNOWLEDGMENTS

This work was supported by an AWWA Abel Wolman graduate research fellowship to R.H.L. and research grants from the Bill and Melinda Gates Foundation and the Virginia Tech Institute for Critical Technology and Applied Science (ICTAS). We thank Dr. Weinan Leng, Dr. Matt Hull, and Jason Jones for particle synthesis and characterization and Matt Chan for DLVO insight and spreadsheets.

■ REFERENCES

(1) Li, X.; Ballerini, D. R.; Shen, W. A Perspective on Paper-Based Microfluidics: Current Status and Future Trends. *Biomicrofluidics* **2012**, *6*, 011301−13.

(2) Ngo, Y. H.; Li, D.; Simon, G. P.; Garnier, G. Paper Surfaces Functionalized by Nanoparticles. *Adv. Colloid Interface Sci.* **2011**, *163*, 23−38.

(3) Govindarajan, A. V.; Ramachandran, S.; Vigil, G. D.; Yager, P.; Bohringer, K. F. A Low Cost Point-of-Care Viscous Sample Preparation Device for Molecular Diagnosis in the Developing World: An Example of Microfluidic Origami. *Lab Chip* **2012**, *12*, 174−181.

(4) Yu, W. W.; White, I. M. A Simple Filter-Based Approach to Surface Enhanced Raman Spectroscopy for Trace Chemical Detection. *Analyst* **2012**, *137*, 168−173.

(5) Tomazelli Coltro, W. K.; Cheng, C. M.; Carrilho, E.; de Jesus, D. P. Recent Advances in Low-cost Microfluidic Platforms for Diagnostic Applications. *Electrophoresis* **2014**, *35*, 2309−2324.

(6) Wong, T. S.; Chen, T.-H.; Shen, X.; Ho, C. M. Nanochromatography Driven by the Coffee Ring Effect. *Anal. Chem.* **2011**, *83*, 1871−1873.

(7) Petosa, A. R.; Jaisi, D. P.; Quevedo, I. R.; Elimelech, M.; Tufenkji, N. Aggregation and Deposition of Engineered Nanomaterials in Aquatic Environments: Role of Physicochemical Interactions. *Environ. Sci. Technol.* **2010**, *44*, 6532−6549.

(8) Gesenhues, U. The Mechanism of Polyelectrolyte-assisted Retention of TiO_2 Filler Particles During Paper Formation. *Adv. Colloid Interface Sci.* **2011**, *162*, 1−21.

(9) Pelletier, M. J. *Analytical Applications of Raman Spectroscopy*; Blackwell Science: Malden, MA, 1999.

(10) Moskovits, M. Surface-Enhanced Spectroscopy. *Rev. Mod. Phys.* **1985**, *57*, 783−826.

(11) Homola, J. Surface Plasmon Resonance Sensors for Detection of Chemical and Biological Species. *Chem. Rev.* **2008**, *108*, 462−493.

(12) Daniel, M. C.; Astruc, D. Gold Nanoparticles: Assembly, Supramolecular Chemistry, Quantum-Size-Related Properties, and Applications Toward Biology, Catalysis, and Nanotechnology. *Chem. Rev.* **2003**, *104*, 293−346.

(13) Halvorson, R. A.; Vikesland, P. J. Surface-Enhanced Raman Spectroscopy (SERS) for Environmental Analyses. *Environ. Sci. Technol.* **2010**, *44*, 7749−7755.

(14) Haynes, C. L.; McFarland, A. D.; Van Duyne, R. P. Surface-Enhanced Raman Spectroscopy. *Anal. Chem.* **2005**, *77*, 338A−246A.

(15) Wang, Y.; Yan, B.; Chen, L. SERS Tags: Novel Optical Nanoprobes for Bioanalysis. *Chem. Rev.* **2013**, *113*, 1391−1428.

(16) Kneipp, J.; Kneipp, H.; Kneipp, K. SERS—A Single-Molecule and Nanoscale Tool for Bioanalytics. *Chem. Soc. Rev.* **2008**, *37*, 1052−1060.

(17) Kneipp, K.; Haka, A. S.; Kneipp, H.; Badizadegan, K.; Yoshizawa, N.; Boone, C.; Shafer-Peltier, K. E.; Motz, J. T.; Dasari, R. R.; Feld, M. S. Surface-Enhanced Raman Spectroscopy in Single Living Cells Using Gold Nanoparticles. *Appl. Spectrosc.* **2002**, *56*, 150−154.

(18) Wark, A. W.; Stokes, R. J.; Darby, S. B.; Smith, W. E.; Graham, D. Dynamic Imaging Analysis of SERS-Active Nanoparticle Clusters in Suspension. *J. Phys. Chem. C* **2010**, *114*, 18115−18120.

(19) Ando, J.; Yano, T.; Fujita, K.; Kawata, S. Metal Nanoparticles for Nano-imaging and Nano-analysis. *Phys. Chem. Chem. Phys.* **2013**, *15*, 13713−13722.

(20) Abbas, A.; Brimer, A.; Slocik, J. M.; Tian, L.; Naik, R. R.; Singamaneni, S. Multifunctional Analytical Platform on a Paper Strip: Separation, Preconcentration, and Subattomolar Detection. *Anal. Chem.* **2013**, *85*, 3977−3983.

(21) Tsai, T. T.; Shen, S.-W.; Cheng, C. M.; Chen, C. F. Paper-Based Tuberculosis Diagnostic Devices with Colorimetric Gold Nanoparticles. *Sci. Technol. Adv. Mater.* **2013**, *14*, No. 044404.

(22) Li, B.; Zhang, W.; Chen, L.; Lin, B. A Fast and Low-cost Spray Method for Prototyping and Depositing Surface-enhanced Raman Scattering Arrays on Microfluidic Paper Based Device. *Electrophoresis* **2013**, *34*, 2162−2168.

(23) Halvorson, R. A.; Vikesland, P. J. Drop Coating Deposition Raman (DCDR) for Microcystin-LR Identification and Quantitation. *Environ. Sci. Technol.* **2011**, *45*, 5644−5651.

(24) Carrilho, E.; Phillips, S. T.; Vella, S. J.; Martinez, A. W.; Whitesides, G. M. Paper Microzone Plates. *Anal. Chem.* **2009**, *81*, 5990−5998.

(25) Carrilho, E.; Martinez, A. W.; Whitesides, G. M. Understanding Wax Printing: A Simple Micropatterning Process for Paper-Based Microfluidics. *Anal. Chem.* **2009**, *81*, 7091−7095.

(26) Frens, G. Controlled Nucletion for the Regulation of the Particle Size in Monodiperse Gold Suspensions. *Nature, Phys. Sci.* **1973**, *241*, 20−22.

(27) Hull, M. S.; Chaurand, P.; Rose, J.; Auffan, M.; Bottero, J. Y.; Jones, J. C.; Schultz, I. R.; Vikesland, P. J. Filter-Feeding Bivalves Store and Biodeposit Colloidally Stable Gold Nanoparticles. *Environ. Sci. Technol.* **2011**, *45*, 6592−6599.

(28) Brown, K. R.; Walter, D. G.; Natan, M. J. Seeding of Colloidal Au Nanoparticle Solutions. 2. Improved Control of Particle Size and Shape. *Chem. Mater.* **1999**, *12*, 306−313.

(29) Ao, L. M.; Gao, F.; Pan, B. F.; Cui, D. X.; Gu, H. C. Interaction Between Gold Nanoparticles and Bovine Serum Albumin or Sheep Antirabbit Immunoglobulin G. *Chin. J. Chem.* **2006**, *24*, 253−256.

(30) Qian, X.; Peng, X.-H.; Ansari, D. O.; Yin-Goen, Q.; Chen, G. Z.; Shin, D. M.; Yang, L.; Young, A. N.; Wang, M. D.; Nie, S. In Vivo Tumor Targeting and Spectroscopic Detection with Surface-enhanced Raman Nanoparticle Tags. *Nat. Biotechnol.* **2008**, *26*, 83−90.

DOI: 10.1021/acsami.5b01192
ACS Appl. Mater. Interfaces 2015, 7, 9139−9146

(31) Kennedy, A. J.; Hull, M. S.; Bednar, A. J.; Goss, J. D.; Gunter, J. C.; Bouldin, J. L.; Vikesland, P. J.; Steevens, J. A. Fractionating Nanosilver: Importance for Determining Toxicity to Aquatic Test Organisms. *Environ. Sci. Technol.* **2010**, *44*, 9571−9577.
(32) Ma, R.; Levard, C.; Marinakos, S. M.; Cheng, Y.; Liu, J.; Michel, F. M.; Brown, G. E.; Lowry, G. V. Size-controlled Dissolution of Organic-coated Silver Nanoparticles. *Environ. Sci. Technol.* **2011**, *46*, 752−759.
(33) Song, J. E.; Phenrat, T.; Marinakos, S.; Xiao, Y.; Liu, J.; Wiesner, M. R.; Tilton, R. D.; Lowry, G. V. Hydrophobic Interactions Increase Attachment of Gum Arabic- and PVP-Coated Ag Nanoparticles to Hydrophobic Surfaces. *Environ. Sci. Technol.* **2011**, *45*, 5988−5995.
(34) Silvert, P.-Y.; Herrera-Urbina, R.; Duvauchelle, N.; Vijayakrishnan, V.; Elhsissen, K. T. Preparation of Colloidal Silver Dispersions by the Polyol Process. Part 1-Synthesis and Characterization. *J. Mater. Chem.* **1996**, *6*, 573−577.
(35) Gao, P.; Weaver, M. J. Surface-Enhanced Raman Spectroscopy as a Probe of Adsorbate-Surface Bonding: Benzene and Monosubstituted Benzenes Adsorbed at Gold Electrodes. *J. Phys. Chem.* **1985**, *89*, 5040−5046.
(36) Gao, P.; Weaver, M. J. Metal-Adsorbate Vibrational Frequencies as a Probe of Surface Bonding: Halides and Pseudohalides at Gold Electrodes. *J. Phys. Chem.* **1986**, *90*, 4057−4063.
(37) Matthaus, C.; Chernenko, T.; Miljkovic, M.; Diem, M. *Biomedical Applications of Confocal Raman Micro-Spectroscopy: Label-Free Monitoring of Subcellular Organelles and Drug Uptake*; WiTec Workshop, Introduction to Confocal Raman Microscopy: Ulm, Germany, 2008.
(38) Toomre, D.; Pawley, J. B., In *Handbook of Biological Confocal Microscopy*, 3rd ed.; Pawley, J. B., Ed.; Springer: New York, 2006; Chapter 10, pp 221−238.
(39) Qing, S. In *Model Cellulosic Surfaces*; Roman, M., Ed.; American Chemical Society: Washington D.C., 2009; Chapter 12, pp 259−289.
(40) Dagaonkar, M.; Majumdar, U. Effect of Fluid Flow, Solution Chemistry and Surface Morphology of Fibrous Material on Colloid Filtration. *J. Eng. Fibers Fabr.* **2012**, *7*, 62−74.
(41) Lu, Y.; Shi, W.; Jiang, L.; Qin, J.; Lin, B. Rapid Prototyping of Paper-based Microfluidics With Wax for Low-Cost, Portable Bioassay. *Electrophoresis* **2009**, *30*, 1497−1500.
(42) Martinez, A. W.; Phillips, S. T.; Whitesides, G. M.; Carrilho, E. Diagnostics for the Developing World: Microfluidic Paper-Based Analytical Devices. *Anal. Chem.* **2010**, *82*, 3−10.
(43) Kreze, T.; Stana-Kleinschek, K.; Ribitsch, V. The Sorption Behaviour of Cellulose Fibres. *Lenzinger Ber.* **2001**, *80*, 28−33.
(44) Ahuja, S. *Chromatography and Separation Science*; Academic Press: Amsterdam, 2003.
(45) Wiley, J. H.; Atalla, R. H. Band Assignments in the Raman Spectra of Celluloses. *Carbohydr. Res.* **1987**, *160*, 113−129.
(46) Vincent, W. F. Fluorescence Properties of the Freshwater Phytoplankton: Three Algal Classes Compared. *Br. Phycological J.* **1983**, *18*, 5−21.
(47) Sadler, P. J.; Tucker, A. pH-induced Structural Transitions of Bovine Serum Albumin. *Eur. J. Biochem.* **1993**, *212*, 811−817.
(48) Levy, Y.; Onuchic, J. N. Water and Proteins: A Love−Hate Relationship. *Proc. Natl. Acad. Sci. U. S. A.* **2004**, *101*, 3325−3326.
(49) Dalgaard, P. *Introductory Statistics with R*, 2nd ed.; Springer: New York, 2008.
(50) Jiang, J.; Oberdörster, G.; Biswas, P. Characterization of Size, Surface Charge, and Agglomeration State of Nanoparticle Dispersions for Toxicological Studies. *J. Nanopart. Res.* **2009**, *11*, 77−89.
(51) van Oss, C. J. *Interfacial Forces in Aqueous Media*, 2nd ed.; Taylor & Francis: Boca Raton, FL, 2006.
(52) Israelachvili, J. N. *Intermolecular and Surface Forces*, 3rd ed.; Elsevier: Burlington, MA, 2011.
(53) Derjaguin, B. V.; Landau, L. Theory of the Stability of Strongly Charged Lyophobic Sols and of the Adhesion of Strongly Charged Particles in Solutions of Electrolytes. *Acta Phys. Chem.* **1941**, *14*, 633−662.
(54) Lifshitz, E. M. The Theory of Molecular Attractive Forces Between Solids. *Sov. Phys.* **1956**, *2*, 73−83.
(55) Adamczyk, Z.; Weroński, P. Application of the DLVO Theory for Particle Deposition Problems. *Adv. Colloid Interface Sci.* **1999**, *83*, 137−226.
(56) Jaycock, M. J.; Pearson, J. L. A Study of the Retention of Pigment During Paper Formation. *J. Colloid Interface Sci.* **1976**, *55*, 181−190.
(57) Eijkel, J. T.; Berg, A. Nanofluidics: What Is It and What Can We Expect From It? *Microfluid. Nanofluid.* **2005**, *1*, 249−267.
(58) Pelton, A. Model of the External Surface of Wood Pulp Fibers. *Nord. Pulp Pap. Res. J.* **1993**, *08*, 113−119.
(59) Michen, B.; Meder, F.; Rust, A.; Fritsch, J.; Aneziris, C.; Graule, T. Virus Removal in Ceramic Depth Filters Based on Diatomaceous Earth. *Environ. Sci. Technol.* **2011**, *46*, 1170−1177.
(60) Panwar, V.; Kang, B.-S.; Park, J.-O.; Park, S.-H. New Ionic Polymer−Metal Composite Actuators Based on PVDF/PSSA/PVP Polymer Blend Membrane. *Polym. Eng. Sci.* **2011**, *51*, 1730−1741.
(61) Wu, M.; Yuan, Y. Molecular Composites of Polyimide/Poly-*n*-vinylpyrrolidone by In-Situ Polycondensation. *Macromol. Symp.* **1997**, *122*, 383−386.
(62) Webb, G. A.; Kamienska-Trela, K.; Aliev, A. E. *Nuclear Magnetic Resonance*; Royal Society of Chemistry: Cambridge, U.K., 2010.
(63) Masson, J.-F. Cellulose/Synthetic-Polymer Blends. Ph.D. Thesis, McGill University, Montréal, Quebec, Canada, 1990.
(64) Jeon, S. I.; Lee, J. H.; Andrade, J. D.; De Gennes, P. G. Protein—Surface Interactions in the Presence of Polyethylene Oxide: I. Simplified Theory. *J. Colloid Interface Sci.* **1991**, *142*, 149−158.
(65) Prime, K. L.; Whitesides, G. M. Adsorption of Proteins Onto Surfaces Containing End-Attached Oligo(Ethylene Oxide): A Model System Using Self-assembled Monolayers. *J. Am. Chem. Soc.* **1993**, *115*, 10714−10721.
(66) El Badawy, A. M.; Scheckel, K. G.; Suidan, M.; Tolaymat, T. The Impact of Stabilization Mechanism on the Aggregation Kinetics of Silver Nanoparticles. *Sci. Total Environ.* **2012**, *429*, 325−331.
(67) Huynh, K. A.; Chen, K. L. Aggregation Kinetics of Citrate and Polyvinylpyrrolidone Coated Silver Nanoparticles in Monovalent and Divalent Electrolyte Solutions. *Environ. Sci. Technol.* **2011**, *45*, 5564−5571.
(68) Sperling, R. A.; Parak, W. J. Surface Modification, Functionalization and Bioconjugation of Colloidal Inorganic Nanoparticles. *Philos. Trans. R. Soc., A* **2010**, *368*, 1333−1383.
(69) Sperling, R. A.; Liedl, T.; Duhr, S.; Kudera, S.; Zanella, M.; Lin, C. A. J.; Chang, W. H.; Braun, D.; Parak, W. J. Size Determination of (Bio)Conjugated Water-Soluble Colloidal Nanoparticles: A Comparison of Different Techniques. *J. Phys. Chem. C* **2007**, *111*, 11552−11559.
(70) Bharkatiya, M.; Nema, R. K.; Bhatnagar, M. Designing and Characterization of Drug Free Patches for Transdermal Application. *Int. J. Pharm. Sci. Drug Res.* **2010**, *2*, 35−39.
(71) Widjaja, E.; Garland, M. Reverse Engineering of Multi-Layer Films. *Mater. Today* **2011**, *14*, 114−117.
(72) Widjaja, E.; Teh, S. Y.; Garland, M. Characterizing Diffusion and Transport in Microfluidics Channels: A Combined Raman Microscopy and Band-target Entropy Minimization Study. *Appl. Spectrosc.* **2012**, *66*, 1226−1232.

DOI: 10.1021/acsami.5b01192
ACS Appl. Mater. Interfaces 2015, 7, 9139−9146